

Enhancing photocatalytic activity of disorder-engineered C/TiO<sub>2</sub> and TiO<sub>2</sub> nanoparticles†Cite this: *J. Mater. Chem. A*, 2014, 2, 7439

Shu Wang, Lei Zhao, Lina Bai, Junmin Yan, Qing Jiang and Jianshe Lian\*

We demonstrate a simple and green synthetic pathway to prepare TiO<sub>2</sub>–carbon nanoparticles (C/TiO<sub>2</sub> NPs) by the sol–gel method, abandoning additional carbon sources but utilizing the organic group in the Ti precursor. Then the C/TiO<sub>2</sub> NPs were decarburized under an air atmosphere at 500 °C for 2 h to form the reduced TiO<sub>2</sub> nanoparticles. XRD, Raman spectrum, HRTEM and electron energy loss spectrum (EELS) analyses showed that the C/TiO<sub>2</sub> NPs were composites of core-shell structured TiO<sub>2</sub> and amorphous carbon; and both C/TiO<sub>2</sub> and reduced TiO<sub>2</sub> NPs contained a large number of oxygen vacancies, which led to structural disorders in them. These structural disorders induced the valence band tails to enhance visible light absorption and to tailor the bandgap structures of the two modified TiO<sub>2</sub> samples to match the hydrogen and oxygen production energy levels. As a result, the two structure-disordered C/TiO<sub>2</sub> and reduced TiO<sub>2</sub> nanocrystals showed excellent solar-driven photocatalytic activities: the C/TiO<sub>2</sub> performed best on the photodegradation of phenol and methyl blue, while the reduced TiO<sub>2</sub> displayed an excellent hydrogen generation rate, 10 times higher than that of the reference TiO<sub>2</sub> by photo-splitting water.

Received 21st January 2014

Accepted 21st March 2014

DOI: 10.1039/c4ta00354c

www.rsc.org/MaterialsA

## Introduction

Semiconductor photocatalysis begins with the activation of photogenerated carriers, and these excited carriers may transfer to the surface to initiate photocatalytic reactions.<sup>1–3</sup> TiO<sub>2</sub>, as a widely used wide band-gap semiconductor, has been extensively studied owing to its abundance, nontoxicity, and stability.<sup>4–7</sup> However, the rapid combination of an electron–hole pair (e<sup>−</sup>/h<sup>+</sup>) dominates the photocatalytic reactions and ordinary anatase phase TiO<sub>2</sub> only absorbs ultraviolet light from the solar spectrum.<sup>8</sup> For practical applications, there have mainly been two ways to improve the photocatalytic activity of TiO<sub>2</sub>, one is by prolonging the lifetime of these photo-carriers or suppressing the combination of photogenerated electron–hole pairs, and the other is by enhancing the solar energy conversion by band-gap engineering. Therefore, numerous efforts have been devoted to improving the optical response and photocatalytic activity of TiO<sub>2</sub> over the entire solar spectral range, and a certain amount of progress has been made.<sup>9–12</sup> Recently, two kinds of “black TiO<sub>2</sub>” aimed at solving the above problems have been proposed and have aroused great attention. One black TiO<sub>2</sub> is the composite of TiO<sub>2</sub> commixing with black-colored carbon species such as graphene.<sup>13–15</sup> Several reports on physical black-colored carbon species/TiO<sub>2</sub> composites have confirmed their

excellent abilities for photogenerated carrier transfer improving the photocatalytic activity.<sup>16,17</sup> Recently, research has importantly suggested that TiO<sub>2</sub>–graphene is in essence the same as other TiO<sub>2</sub>–carbon composite materials on enhancement of photocatalytic activity.<sup>18</sup> Another black-colored TiO<sub>2</sub> is an innovative modification of TiO<sub>2</sub> by introducing surface disorder to narrow the bandgap of TiO<sub>2</sub> nanocrystals and to increase the visible and near infrared (Vis–NIR) optical absorption.<sup>19–21</sup> These chemically disorder-engineered TiO<sub>2</sub> nanocrystals significantly adjust the band structure to fit the redox potential of water in the photocatalytic water-splitting process, thus they possess the ability to produce H<sub>2</sub> with considerable efficiency.<sup>19,21</sup> However, the strategies for preparing “black TiO<sub>2</sub>” materials have a number of limitations such as multiple steps, harsh synthesis conditions, or require expensive facilities for the modification process.<sup>13–22</sup>

In the present work, we proposed an economical and green synthetic pathway using the traditional sol–gel technique, abandoning additional carbon sources but utilizing the organic group in the Ti precursor, to prepare nanostructured TiO<sub>2</sub>–carbon core-shell composites. These C/TiO<sub>2</sub> nanoparticles (NPs) should have two advantages: the covered carbon layers may support the effective separation of photogenerated electron/hole pairs, and the disorders induced in the TiO<sub>2</sub> lattice may improve the visible light response of TiO<sub>2</sub> crystals; hence, the modified TiO<sub>2</sub>–carbon composite should exhibit significant advances in solar-driven photocatalytic performance and provide a simple way for modification of the semiconductor photocatalyst. Furthermore, we decarburized the TiO<sub>2</sub>–carbon

Key Lab of Automobile Materials, Ministry of Education, College of Materials Science and Engineering, Jilin University, Nanling Campus, Changchun, 130025, P.R. China. E-mail: lianjs@jlu.edu.cn; Fax: +86-431-85095876; Tel: +86-431-85095876

† Electronic supplementary information (ESI) available. See DOI: 10.1039/c4ta00354c

composite by annealing it in air to obtain defect-engineered  $\text{TiO}_2$  with only structural disorders, which should also have enhanced photocatalytic performance. The structures of the  $\text{TiO}_2$ -carbon composite and its decarburization product were characterized and their solar-driven photocatalytic activities in the degradation of organic pollutants (phenol and methylene blue) and  $\text{H}_2$  production were investigated.

## Preparations

The samples were prepared by the sol-gel technique using a typical synthetic procedure. A precursor solution was prepared consisting of tetrabutyl titanate, ethanol, hydrochloric acid and deionized water. After aging the solution for 48 h at room temperature to form gels, the gels were dried at  $80^\circ\text{C}$  for 12 h to form dried powder. According to the general sol-gel process, part of the powder was calcinated at  $500^\circ\text{C}$  in air to form ordinary  $\text{TiO}_2$  powder as a reference sample.

As a modification, nitrogen gas was passed through a quartz tube to dilute oxygen to the correct level, hence a C-rich (called C/ $\text{TiO}_2$ ) powder was obtained by calcinating at  $500^\circ\text{C}$  in the  $\text{N}_2$  atmosphere. For the C/ $\text{TiO}_2$ , carbon layers were obtained by carbonization of the alkoxy group ( $-\text{OC}_4\text{H}_9$ ) in the Ti precursor ( $\text{Ti}(\text{OC}_4\text{H}_9)_4$ ) in an anoxic environment (S1). Consequently, the C/ $\text{TiO}_2$  was further calcinated at  $500^\circ\text{C}$  for 2 h in air to form the decarburized  $\text{TiO}_2$ , called reduced  $\text{TiO}_2$ . All of the thermal treatments were carried out using a heating rate of  $10^\circ\text{C min}^{-1}$  in a tube furnace. So there were three  $\text{TiO}_2$  samples: reference  $\text{TiO}_2$ , C/ $\text{TiO}_2$  and reduced  $\text{TiO}_2$ , and then their structure characterization (S2) and photocatalytic performance (S3) were investigated.

## Results and discussion

Fig. 1 shows the XRD patterns of the three samples. They are all anatase phase with no other phase detected. The Full Width Half Maximum (FWHM) of the C/ $\text{TiO}_2$  and reduced  $\text{TiO}_2$  samples is wider than that of the reference  $\text{TiO}_2$ , which, using

the Scherrer equation, gives estimations of the average grain size to be 23, 9, and 13 nm for reference  $\text{TiO}_2$ , C/ $\text{TiO}_2$  and reduced  $\text{TiO}_2$  NPs, respectively. The modified synthetic procedure produces C/ $\text{TiO}_2$  and reduced  $\text{TiO}_2$  NPs with much smaller average grain sizes than the reference  $\text{TiO}_2$  hence with larger surface areas, which should be favorable for photocatalytic performance. The inset figure shows that the estimated lattice strain evidently increases with decreasing average grain size. Refined structural parameters (Table S1†) calculated from the XRD spectra show no evident volume difference (less than 0.3%) among these powders, so the increased lattice strain (reaching about 1.3%) is mainly attributed to severe lattice distortion.

The structural properties of the synthesized  $\text{TiO}_2$  were further examined by measuring their Raman scattering, as shown in Fig. 2. All three samples show the anatase  $\text{TiO}_2$  vibrational spectrum with six Raman-active fundamentals ( $E_{g(1)}$ ,  $E_{g(2)}$  and  $E_{g(3)}$  at 141, 192, and  $638\text{ cm}^{-1}$ ,  $B_{1g(1)}$  and  $B_{1g(2)}$  at 395 and  $514\text{ cm}^{-1}$ , and  $A_{1g(1)}$  mode at  $514\text{ cm}^{-1}$ , respectively), indicating the existence of anatase  $\text{TiO}_2$  in these samples, which is in agreement with the XRD results. The Raman spectrum of the C/ $\text{TiO}_2$  powder is different from those of the other two samples: two intense characteristic peaks of graphite-like carbon, D-band and G-band, centered at  $1373$  and  $1602\text{ cm}^{-1}$ , respectively, appear in the C/ $\text{TiO}_2$  sample. The G-band at  $1602\text{ cm}^{-1}$  confirms the presence of  $\text{sp}^2$  carbon-type structure in the C/ $\text{TiO}_2$  particles,<sup>23</sup> while the D-band at around  $1373\text{ cm}^{-1}$  is attributed to the presence of defects within the hexagonal graphitic structure.<sup>16</sup>

Fig. 3(a)–(c) show high resolution TEM (HRTEM) images of the reference  $\text{TiO}_2$ , C/ $\text{TiO}_2$  and reduced  $\text{TiO}_2$  NPs, respectively, and their corresponding Fourier-filtered images are displayed as inserts. Reference  $\text{TiO}_2$  shows a regular arrangement of its lattice, while the Fourier-filtered images (insets b1 and c1 in Fig. 3(b) and (c), respectively) of the C/ $\text{TiO}_2$  and reduced  $\text{TiO}_2$  clearly show severe lattice distortions, and some develop into dislocations in selected areas. The severity of the disorders could also be proved by lattice strain calculated from XRD. The located images (insets b2 and b3) clearly show the core-shell

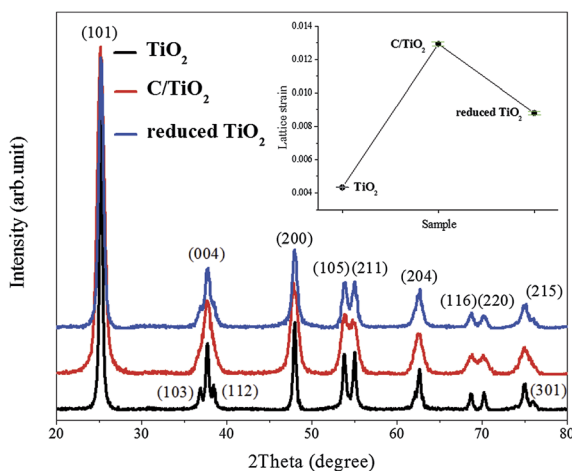


Fig. 1 XRD patterns of the three  $\text{TiO}_2$  samples; a comparison of their lattice strain is shown in the insert.

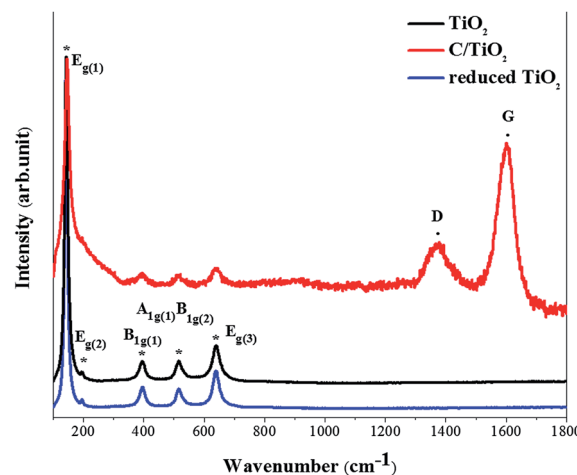


Fig. 2 Raman spectra of the reference  $\text{TiO}_2$ , C/ $\text{TiO}_2$  and reduced  $\text{TiO}_2$  NPs.

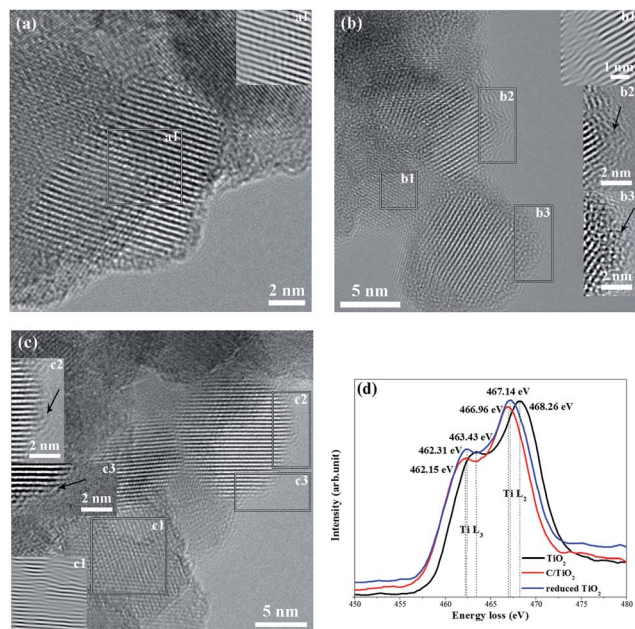


Fig. 3 HRTEM micrographs of (a) reference TiO<sub>2</sub>, (b) C/TiO<sub>2</sub> and (c) reduced TiO<sub>2</sub>, along with Fourier-filtered images (a1, b1 and c1) of selected areas and local enlarged images (b2, b3 and c2, c3) shown as inserts. (d) EELS spectra of the Ti L<sub>2,3</sub> edge for the three samples.

morphology of C/TiO<sub>2</sub> with a  $\sim 1.5$  nm thick amorphous carbon layer, and the carbon layer completely disappears in the reduced TiO<sub>2</sub> NP after decarburization (shown in insets c2 and c3). The carbon shell acts as a barrier on the grain boundary to obstruct the growth of anatase TiO<sub>2</sub> to result in a decrease in crystal size (9 nm). The reduced TiO<sub>2</sub> shows minor secondary growth after decarburization (13 nm) according to the XRD calculated grain size.

Electron energy loss near edge structure (ELNES) appears above the absorption edge in the electron energy loss spectrum (EELS), which is sensitive to the unoccupied valence band and could be used to interpret the electronic states qualitatively. Fig. 3(d) shows a comparison of the Ti L-edge ELNES of the EELS spectra (Fig. S1†) of the three samples. Ti L<sub>2,3</sub> edges are the main features of the TiO<sub>2</sub> spectrum and allow a qualitative measurement of the chemical state of elemental Ti. The L<sub>3</sub> and L<sub>2</sub> lines are the transitions from  $2p_{3/2}$  to  $3d_{3/2}3d_{5/2}$  and from  $2p_{1/2}$  to  $3d_{3/2}$ , respectively, and their intensities are related to the unoccupied states in the 3d bands.<sup>24,25</sup> From Fig. 3(d), the Ti L<sub>2,3</sub> edges of reference TiO<sub>2</sub>, C/TiO<sub>2</sub> and reduced TiO<sub>2</sub> NPs are 463.43 eV vs. 462.15 eV vs. 462.31 eV in L<sub>3</sub> and 468.26 eV vs. 466.96 eV vs. 467.14 eV in L<sub>2</sub>, respectively, *i.e.*, a decrease in the chemical state energy of Ti is observed in C/TiO<sub>2</sub> and reduced TiO<sub>2</sub> NPs. For the Ti L<sub>2,3</sub> edges ELNES, Ti ions with a higher valence would locate at a higher energy edge, therefore the results demonstrate the average decrease in Ti valence state in both C/TiO<sub>2</sub> and reduced TiO<sub>2</sub> NPs, which implies a mixture of Ti<sup>4+</sup> with a certain quantity of Ti<sup>3+</sup>.<sup>20</sup> In fact, the C/TiO<sub>2</sub> and reduced TiO<sub>2</sub> were prepared in an oxygen-deficient atmosphere, hence, they should have more oxygen vacancies/V<sub>OS</sub> (*i.e.* TiO<sub>2-x</sub>), and the appearance of Ti<sup>3+</sup> ions should be normal.<sup>26,27</sup>

The existence of V<sub>OS</sub> results in lattice contraction as testified by the decrease in lattice parameters from the above XRD analysis and the lattice distortion or dislocations from the HRTEM observation. So, combined consideration of the XRD, HRTEM and EELS studies confirms that the C/TiO<sub>2</sub> and reduced TiO<sub>2</sub> have more V<sub>OS</sub> and a certain quantity of Ti<sup>3+</sup> in their TiO<sub>2</sub> lattices. In addition, the EELS spectrum for C K-edge ELNES of C/TiO<sub>2</sub> proves that the carbon shell exists as amorphous carbon by its ELNES fingerprints as shown in Fig. S1(b).†

The photocatalytic activities of the three synthesized catalysts were evaluated from the degradation of phenol and methylene blue (MB) solutions using a simulated solar light source (see ESI in S3†). Fig. 4(a) and S3† show that both C/TiO<sub>2</sub> and reduced TiO<sub>2</sub> NPs exhibit significant enhancement in solar-driven photocatalytic activity in comparison with the reference TiO<sub>2</sub>, and C/TiO<sub>2</sub> shows the best performance: MB was decomposed in 30 min (Fig. S3†) and phenol was decomposed in 80 min (Fig. 4(a)), while only 20% of MB or phenol was decomposed by the reference TiO<sub>2</sub> in the corresponding intervals. The obvious advantage of C/TiO<sub>2</sub> on photodegradation of MB solution can be attributed to the adsorption of carbon layers on the dye, compared with the degradation of phenol solution.

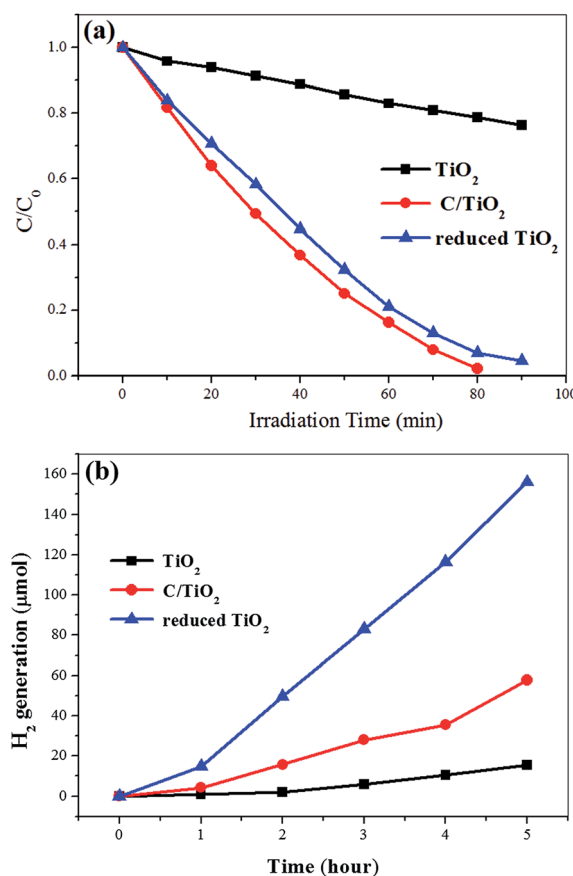


Fig. 4 Comparison of the simulated solar-driven photocatalytic activities of the reference TiO<sub>2</sub>, C/TiO<sub>2</sub> and reduced TiO<sub>2</sub> nanocrystals under the same experimental conditions. (a) Phenol decomposition with time for the three samples. (b) Hydrogen (H<sub>2</sub>) generation with time for the three samples.

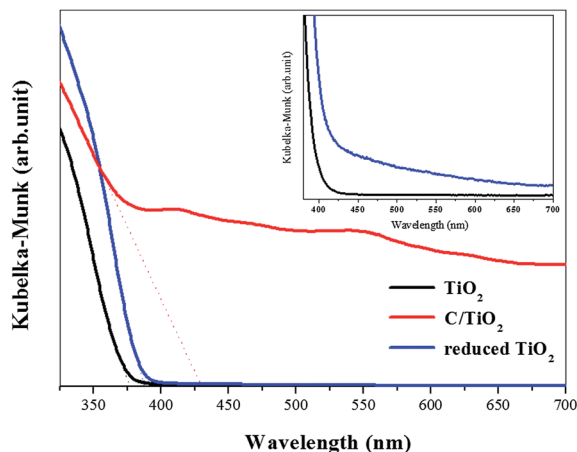


Fig. 5 UV-visible diffuse reflectance spectra of the three samples, and a detailed comparison between reference  $\text{TiO}_2$  and reduced  $\text{TiO}_2$  is shown as an insert.

The  $\text{C}/\text{TiO}_2$  and reduced  $\text{TiO}_2$  samples also exhibit substantial activity and stability in the photocatalytic production of hydrogen from water-splitting under simulated solar light, which advocates their usability as a new energy source. 20 mg of photocatalyst loaded with 0.6 wt% Pt was placed in a Pyrex glass container filled with a solution of water : methanol (as a sacrificial agent) = 1 : 1 in a closed-gas circulation system, and the  $\text{H}_2$  generated was measured. Hydrogen gas evolution as a function of time using the three  $\text{TiO}_2$  samples as photocatalysts is shown in Fig. 4(b). The reference  $\text{TiO}_2$  displays a stable  $\text{H}_2$  release rate of  $\sim 0.154 \text{ mmol h}^{-1} \text{ g}^{-1}$ , while the  $\text{C}/\text{TiO}_2$  and reduced  $\text{TiO}_2$  NPs evidently show increased  $\text{H}_2$  release rates of  $\sim 0.577 \text{ mmol h}^{-1} \text{ g}^{-1}$  and  $\sim 1.560 \text{ mmol h}^{-1} \text{ g}^{-1}$ , respectively. That is, among the three  $\text{TiO}_2$  NPs, the reduced  $\text{TiO}_2$  NPs shows the best solar-driven hydrogen production rate through water-splitting, and is about 10 times higher than that of the reference  $\text{TiO}_2$ .

Fig. 5 shows the UV-visible absorption spectra of the three samples. First, the spectra of the samples of  $\text{C}/\text{TiO}_2$  and reduced  $\text{TiO}_2$  shift to a longer wavelength, revealing the decrease in their bandgap. The optical bandgap of reference  $\text{TiO}_2$  is 3.3 eV, while those of  $\text{C}/\text{TiO}_2$  and reduced  $\text{TiO}_2$  are 2.9 eV and 3.2 eV, respectively. The significant bandgap narrowing (2.9 eV) of  $\text{C}/\text{TiO}_2$  is mainly attributed to surface C-doping. The C atoms occupying the interstitial sites in the  $\text{TiO}_2$  lattice normally exist in the  $\text{TiO}_2$ /carbon species composites,<sup>18</sup> which leads to a decrease in optical bandgap energy. In addition, the optical absorbance of reduced  $\text{TiO}_2$  in the visible range is obviously enhanced compared with the reference  $\text{TiO}_2$ , as shown by the inset in Fig. 5. It is speculated that the  $\text{TiO}_2$  in  $\text{C}/\text{TiO}_2$  should also have enhanced visible light absorbance, although it is hidden by the high absorption of the surface amorphous carbon layer in the visible region.

Surface chemical bonding of  $\text{TiO}_2$  nanocrystals was detected by X-ray photoelectron spectroscopy (XPS) as shown in Fig. S2.† When compared with the experimentally introduced carbon, the strong signal of XP C 1s at 284.8 eV proves the presence of a

carbon shell in  $\text{C}/\text{TiO}_2$  NPs as shown in Fig. S2(a).† In our work, we have attempted to illustrate the reason for a C-rich layer from the calcination process in the ESI for this study (S1†). Since the content of carbon is considerable, it tends to form a carbon layer coating on the surface of  $\text{TiO}_2$ , instead of doping into the internal  $\text{TiO}_2$  lattice. However, it inevitably enters into the surface lattice of  $\text{TiO}_2$  to act as an interstitial atom, considering the smaller atomic size of C. We think that this type of C-doping exists at the interface between the carbon layer and the  $\text{TiO}_2$  core, and this is also the reason for the decreased optical bandgap of  $\text{C}/\text{TiO}_2$  as Fig. 5 shows. In addition, the great difference in ionic radius between  $\text{C}^{4+}$  (16 pm) and  $\text{Ti}^{4+}$  (61 pm) would not lead C to substitute for Ti in the  $\text{TiO}_2$  matrix; meanwhile, a comparison of XP C 1s spectra of the samples is shown in Fig. S2(a),† and there is also no evidence that the C atom substitutes for an O atom to occupy the  $\text{TiO}_2$  lattice, because no signal for Ti–C bonding is present at  $\sim 282 \text{ eV}$ .<sup>28</sup> XP Ti 2p spectra (Fig. S2(b)†) of  $\text{C}/\text{TiO}_2$  and reduced  $\text{TiO}_2$  exhibit a shift of  $\sim 0.3 \text{ eV}$  to higher energy compared with the reference  $\text{TiO}_2$  sample, which indicates the presence of  $\text{V}_\text{O}$ s in the modified  $\text{TiO}_2$  surface. Since  $\text{V}_\text{O}$  registers as a positive charge ( $\text{V}_\text{O}^{2+}$ ), each of the three nearest-neighbor Ti atoms moves away from the vacancy toward its five remaining O neighbors. This causes shortening of the Ti–O bond length, as well as the increase in bonding energy. Similarly, the fitted peaks of the XPS O 1s spectra (Fig. S2(c)–(e)†) illustrate that the “absorption O” (adsorbed  $\text{O}_2/\text{V}_\text{O}$ s and adsorbed  $\text{H}_2\text{O}/\text{OH}$  groups) abunds on the surface of the modified  $\text{TiO}_2$  samples.

Fig. 6(a)–(c) show valence band XPS (VB-XPS) for the reference  $\text{TiO}_2$ ,  $\text{C}/\text{TiO}_2$  and reduced  $\text{TiO}_2$  NPs, respectively. The reference  $\text{TiO}_2$  displays the characteristic VB density of states (DOS) of  $\text{TiO}_2$ , with the band edge at about 1.23 eV below the Fermi energy (Fig. 6(a)). Since the optical bandgap of reference  $\text{TiO}_2$  is 3.3 eV (Table S1†), the conduction band minimum (CBM) would occur at  $-2.07 \text{ eV}$ .<sup>19</sup> For the VB-XPS of both  $\text{C}/\text{TiO}_2$  and reduced  $\text{TiO}_2$  samples, a notable difference compared with the reference  $\text{TiO}_2$  sample is the presence of a band tail induced by structural disorders. The main absorption onsets in the  $\text{C}/\text{TiO}_2$  and reduced  $\text{TiO}_2$  samples are located at 1.06 and 1.19 eV, respectively, whereas the maximum energies associated with the band tails are at about 0.22 and 0.27 eV, respectively. Therefore, their corresponding CBM should be located at  $-1.84$  and  $-2.01 \text{ eV}$ , respectively. Consequently, the remarkable bandgap narrowing of the modified samples (2.06 vs. 2.28 eV) is caused by the substantial shifts of VB tails, and the values would decrease further due to the predicted CB tailing.<sup>19</sup>

Fig. 7 presents schematic illustrations of the structures of the NPs and the corresponding calculated DOS (band edge) of the three samples, constructed using the experimental data from the UV-vis spectroscopy and the VB-XPS results. The DOS band edge charts for the  $\text{C}/\text{TiO}_2$  and reduced  $\text{TiO}_2$  present a clear illustration of the reasonable bandgap narrowing to enhance the photocatalytic activity. The favorable water-splitting mechanism including the modified reduction and oxidation potentials of both  $\text{C}/\text{TiO}_2$  and reduced  $\text{TiO}_2$  is also displayed.



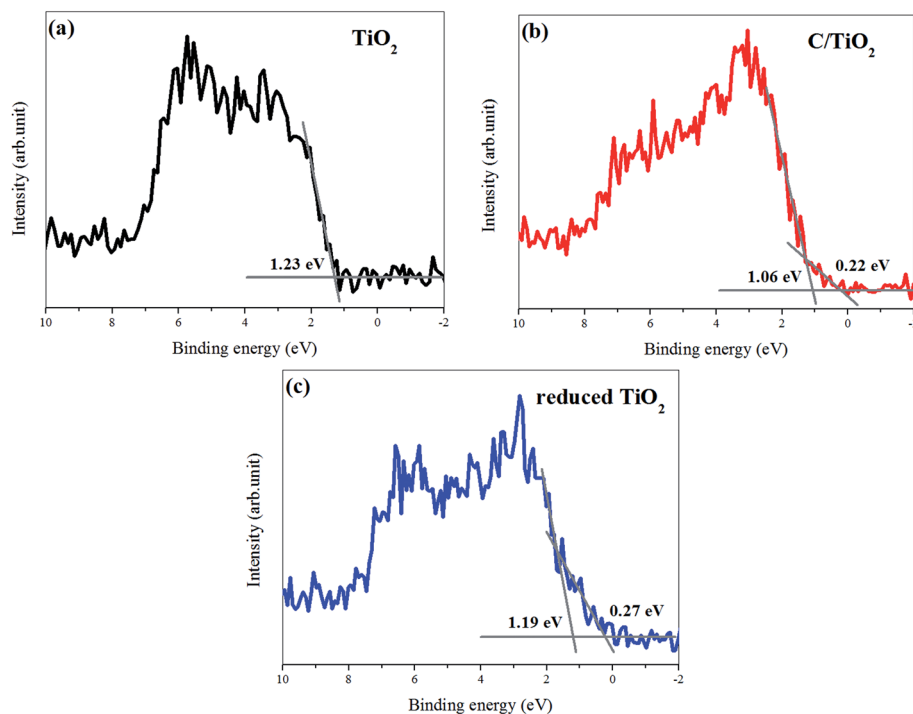


Fig. 6 Valence band XPS spectra of (a) reference  $\text{TiO}_2$ , (b)  $\text{C}/\text{TiO}_2$  and (c) reduced  $\text{TiO}_2$ . The gray auxiliary lines show the linear extrapolation of the curves used to derive the band edge positions of these samples.

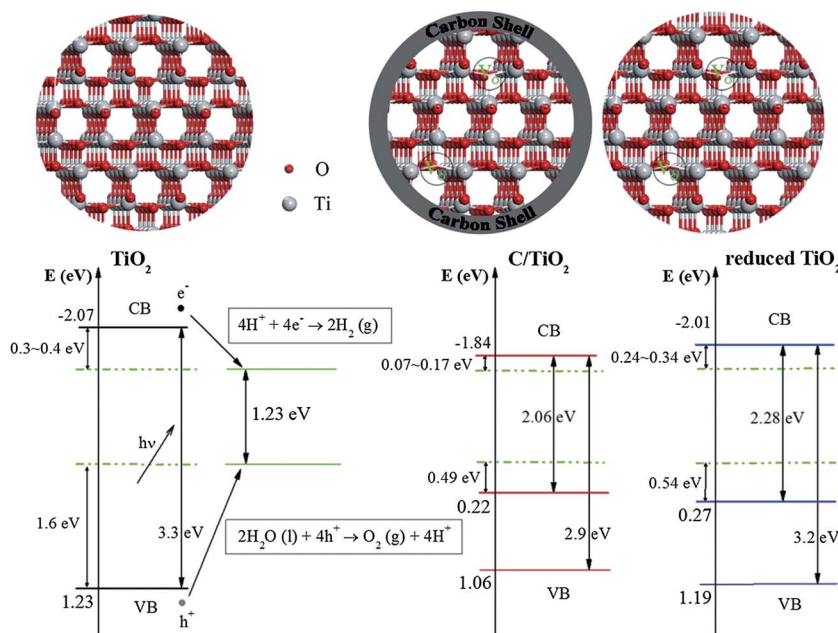


Fig. 7 Schematic illustrations of the nanostructures and the calculated DOSs based on the UV-visible diffuse reflectance spectra and the VB-XPS results, for the reference  $\text{TiO}_2$ ,  $\text{C}/\text{TiO}_2$  and reduced  $\text{TiO}_2$ . The energy of the valence band maximum of the bulk phase is taken to be zero.

The significant bandgap engineering of the modified  $\text{TiO}_2$  samples provides the improvement in photocatalytic activity based on the remark availability of solar energy. Moreover, the dislocations and the lattice distortion in the  $\text{C}/\text{TiO}_2$  and reduced  $\text{TiO}_2$  NPs act as electroactive defects to produce localized band bending. The band bending and the associated

electric field in the space charge region can promote the separation of a photogenerated electron/hole pair.<sup>29,30</sup> For  $\text{C}/\text{TiO}_2$  NPs, the carbon shell makes a further enhancement on inhibiting the electron/hole pair recombination or prolonging the lifetime of charge carriers, in comparison with the reduced  $\text{TiO}_2$  NPs. In the present work, the carbon shell is thin enough to

allow light transmission to the TiO<sub>2</sub> core, and the surface d- $\pi$  conjugation structure of the C/TiO<sub>2</sub> NPs allows the photo-generated electrons to transfer from the conduction band of TiO<sub>2</sub> to the carbon shell.<sup>16,31</sup> Since the carbon shell possesses excellent conductivity of electrons,<sup>31,32</sup> the photogenerated electron/hole pair separates smoothly and then these carriers can rapidly go through the surface photo-oxidation reactions. This is the reason for the better degradation efficiency of C/TiO<sub>2</sub> compared with that of reduced TiO<sub>2</sub> NPs.

To achieve high efficiency for hydrogen production through water-splitting, a desirable photocatalyst should have a bandgap of around 2.0 eV (2.06 vs. 2.28 eV in our work), and the positions of its band edges must match the redox potentials of water.<sup>33</sup> Furthermore, to modify TiO<sub>2</sub> to be a candidate for water splitting, it should not affect the CBM much but increase the valence band maximum (VBM) significantly. In the present work, the band structures of C/TiO<sub>2</sub> and reduced TiO<sub>2</sub> NPs have been modified to greatly increase the VBM, thus both modified samples give obvious improvements in the efficiency of hydrogen production compared with the reference TiO<sub>2</sub> as shown in Fig. 4(b). Notably, reduced TiO<sub>2</sub> NPs display a better H<sub>2</sub> release rate, which is nearly three times and 10 times higher than that of C/TiO<sub>2</sub> and reference TiO<sub>2</sub>, respectively. From Fig. 7, the CBM of reduced TiO<sub>2</sub> is higher than that of C/TiO<sub>2</sub>, which means that the reduction potential of reduced TiO<sub>2</sub> is larger than that of C/TiO<sub>2</sub> in the water-splitting process. The difference in the reduction potential (0.07–0.17 eV vs. 0.24–0.34 eV) between them is 0.17 eV, *i.e.*, the reduction potential of reduced TiO<sub>2</sub> is 0.17 eV higher than that of C/TiO<sub>2</sub>. Meanwhile, the lower VBM of reduced TiO<sub>2</sub> also represents its higher oxidizing potential (0.05 eV) than that of C/TiO<sub>2</sub>. As the optical response ranges of the modified samples are both extended to the visible light region, the reduced TiO<sub>2</sub> sample possesses a much more favorable chemical potential for water-splitting, thus it exhibits a better efficiency in hydrogen production.

## Conclusions

In summary, we have presented an economical and environmentally friendly one-step approach to synthesize core-shell C/TiO<sub>2</sub> nanocrystals with structural disorders. Meanwhile, reduced TiO<sub>2</sub> with similar structural disorders has been obtained through a decarburization process for C/TiO<sub>2</sub> NPs. The structural disorders in the catalysts induce a valence band tail to narrow the bandgap significantly and to tailor the band structure to adapt it to the redox potential of water in the photocatalytic process. The unique morphology and structure enable both modified TiO<sub>2</sub> samples to achieve a visible response and outstanding photocatalytic activities. Having their respective merits, the C/TiO<sub>2</sub> NPs display better photodegradation of water pollutants attributed to the rapid charge transfer of the carbon shell; and the reduced TiO<sub>2</sub> has a much better efficiency in H<sub>2</sub> production as a result of the correct positions of its band edges. The findings of our study may provide a facile way to develop a nanostructurally disordered TiO<sub>2</sub> photocatalyst to enhance photocatalytic activity, to be applied both in water pollution treatment and in the generation of a clean energy source.

## Acknowledgements

This work is supported by the Foundation of National Key Basic Research and Development Program (no. 2010CB631001) and the Program for Changjiang Scholars and Innovative Research Team in University.

## References

- 1 A. Fujishima and K. Honda, *Nature*, 1972, **238**, 37–38.
- 2 A. Fujishima, T. N. Rao and D. A. Tryk, *J. Photochem. Photobiol., C*, 2000, **1**, 1–21.
- 3 D. A. Tryk, A. Fujishima and K. Honda, *Electrochim. Acta*, 2000, **45**, 2363–2376.
- 4 M. Grätzel, *Nature*, 2001, **414**, 338–344.
- 5 A. Hagfeldt and M. Grätzel, *Chem. Rev.*, 1995, **95**, 49–68.
- 6 A. L. Linsebigler, G. Lu and J. T. Yates Jr, *Chem. Rev.*, 1995, **95**, 735–758.
- 7 A. Millis and S. L. Hunte, *J. Photochem. Photobiol., A*, 1997, **108**, 1–35.
- 8 F. Zuo, L. Wang, T. Wu, Z. Y. Zhang, D. Borchardt and P. Y. Feng, *J. Am. Chem. Soc.*, 2010, **132**, 11856–11857.
- 9 G. Jiang, Z. Lin, C. Chen, L. Zhu, Q. Chang, N. Wang, W. Wei and H. Tang, *Carbon*, 2011, **49**, 2693–2701.
- 10 D. Sarkar, C. K. Ghosh, S. Mukherjee and K. K. Chattopadhyay, *ACS Appl. Mater. Interfaces*, 2013, **5**, 331–337.
- 11 Q. Xiang, J. Yu and M. Jaroniec, *J. Am. Chem. Soc.*, 2012, **134**, 6575–6578.
- 12 M. Murdoch, G. I. N. Waterhouse, M. A. Nadeem, J. B. Metson, M. A. Keane, R. F. Howe, J. Llorca and H. Idriss, *Nat. Chem.*, 2011, **3**, 489–492.
- 13 Y. Liang, H. Wang, H. S. Casalongue, Z. Chen and H. Dai, *Nano Res.*, 2010, **10**, 701–705.
- 14 H. Zhang, X. Lv, Y. Li, Y. Wang and J. Li, *ACS Nano*, 2010, **4**, 380–386.
- 15 G. Williams, B. Seger and P. V. Kamat, *ACS Nano*, 2008, **2**, 1487–1491.
- 16 L. W. Zhang, H. B. Fu and Y. F. Zhu, *Adv. Funct. Mater.*, 2008, **18**, 2180–2189.
- 17 L. Zhao, X. Chen, X. Wang, Y. Zhang, W. Wei, Y. Sun, M. Antonietti and M. M. Titirici, *Adv. Mater.*, 2010, **22**, 3317–3321.
- 18 Y. Zhang, Z. Tang, X. Fu and Y. Xu, *ACS Nano*, 2010, **4**, 7303–7314.
- 19 X. Chen, L. Liu, P. Y. Yu and S. S. Mao, *Science*, 2011, **331**, 746–750.
- 20 A. Naldoni, M. Allieta, S. Santangelo, M. Marelli, F. Fabbri, S. Cappelli, C. L. Bianchi, R. Psaro and V. D. Santo, *J. Am. Chem. Soc.*, 2012, **134**, 7600–7603.
- 21 G. Wang, H. Wang, Y. Ling, Y. Tang, X. Yang, R. C. Fitzmorris, C. Wang, J. Z. Zhang and Y. Li, *Nano Lett.*, 2011, **11**, 3026–3033.
- 22 X. Chen, L. Liu, Z. Liu, M. A. Marcus, W. C. Wang, N. A. Oyler, M. E. Grass, B. Mao, P. A. Glans, P. Y. Yu, J. Guo and S. S. Mao, *Sci. Rep.*, 2013, **3**, 1510.
- 23 X. Chen and S. S. Mao, *Chem. Rev.*, 2007, **107**, 2891–2959.

- 24 D. H. Pearson, C. C. Ahn and B. Fultz, *Phys. Rev. B: Solid State*, 1993, **47**, 8471–8478.
- 25 J. H. Paterson and O. L. Krivanek, *Ultramicroscopy*, 1990, **32**, 319–325.
- 26 C. D. Valentin and G. Pacchioni, *J. Phys. Chem. C*, 2009, **113**, 20543–20552.
- 27 E. Finazzi, C. D. Valentin, G. Pacchioni and A. Selloni, *J. Chem. Phys.*, 2008, **129**, 154113.
- 28 L. Zhang and R. V. Koka, *Mater. Chem. Phys.*, 1998, **57**, 23–32.
- 29 D. M. Adams, L. Brus, C. E. D. Chidsey, S. Creager, C. Creutz, C. R. Kagan, P. V. Kamat, M. Lieberman, S. Lindsay, R. A. Marcus, R. M. Metzger, M. E. Michel-Beyerle, J. R. Miller, M. D. Newton, D. R. Rolison, O. Sankey, K. S. Schanze, J. Yardley and X. Zhu, *J. Phys. Chem. B*, 2003, **107**, 6668–6697.
- 30 J. B. Asbury, E. Hao, Y. Wang, H. N. Ghosh and T. Lian, *J. Phys. Chem. B*, 2001, **105**, 4545–4557.
- 31 X. Wang, L. Zhi and K. Müllen, *Nano Lett.*, 2008, **8**, 323–327.
- 32 K. S. Novoselov, A. K. Geim, S. V. Morozov, D. Jiang, Y. Zhang, S. V. Dubonos, I. V. Grigorieva and A. A. Firsov, *Science*, 2004, **306**, 666–669.
- 33 O. Khaselev and J. A. Turner, *Science*, 1998, **280**, 425–427.